High-Fidelity Reconstruction of Approach Deviations: Integrating QAR Flight Data with ILS Electromagnetic Signal Physics

LIU Jiming[1], *GAO Zhenxing*[2*], *LI Yue*[2]

1. College of Civil Aviation, Nanjing University of Aeronautics and Astronautics, Nanjing 211106, P. R. China;
2. College of General Aviation and Flight, Nanjing University of Aeronautics and Astronautics, Nanjing 211106, P. R. China

(Received 12 October 2025; revised 29 January 2026; accepted 15 March 2026)

Abstract: Precise detection of flight path deviations during the approach phase is critical for identifying operational risks and enhancing aviation safety. However, existing monitoring methods often face significant challenges in distinguishing between environmental signal distortions and operational handling errors due to the lack of high-fidelity physical reference models. To address these limitations, this study establishes an integrated simulation framework for required navigation performance (RNP) and instrument landing system (ILS) approaches by synthesizing quick access recorder (QAR) data with rigorous navigation modeling. A site-specific "digital twin" of Linfen Yaodu Airport is constructed, incorporating 3D trajectory reconstruction based on Mercator projection and Baro-VNAV logic, alongside an electromagnetic simulation of ILS signals utilizing antenna array and image theory to model multipath effects. Empirical validation demonstrates that the model accurately reproduces critical signal characteristics, including interference fringes and secondary glide slope lobes. Furthermore, quantitative regression analysis establishes a definitive linear correlation ($R^2 > 0.98$) between the theoretical difference in depth of modulation (DDM) and the pilot-observed distance off track (DOT), providing a verified calibration equation for interpreting cockpit indications. The practical utility of the framework is substantiated through the investigation of a specific vertical deviation anomaly, where the model successfully traces the causal chain from signal distortion to unsafe landing parameters such as threshold height exceedance and flare compression. This research offers a robust, data-driven methodology for continuous flight quality monitoring and provides a scientific foundation for identifying the root causes of navigation incidents.

Key words: flight deviation detection; flight quality monitoring; RNP approach procedure; instrument landing system(ILS)

CLC number: V351 **Document code:** A **Article ID:** 1005-1120(2026)02-0187-16

0 Introduction

With the continuous expansion of the global civil aviation fleet and the increasing density of air traffic, flight safety management faces unprecedented challenges[1]. Statistical data consistently indicates that the approach and landing phases are the most critical segments of flight, accounting for a disproportionately high percentage of accidents and serious incidents globally. Consequently, identifying operational risks and ensuring navigation integrity during these complex phases has become a focal point of aviation safety research[2].

In modern terminal area operations, the integration of required navigation performance (RNP) and the instrument landing system (ILS) has emerged as a dominant paradigm[3]. This hybrid operation leverages the flexibility of RNP for efficient trajectory management and the high precision of ILS

*Corresponding author, E-mail address: z.x.gao@nuaa.edu.cn.

How to cite this article: LIU Jiming, GAO Zhenxing, LI Yue. High-fidelity reconstruction of approach deviations: Integrating QAR flight data with ILS electromagnetic signal physics[J]. Transactions of Nanjing University of Aeronautics and Astronautics, 2026,43(2):187-202.

http://dx.doi.org/10.16356/j.1005-1120.2026.02.003

for the final landing guidance, offering a robust solution for operations in adverse weather and complex terrain environments[4]. However, the reliability of these systems is susceptible to environmental factors, such as electromagnetic interference, multipath effects caused by terrain, and atmospheric turbulence. Traditional methods for validating navigation performance primarily rely on periodic flight inspections. While effective, these inspections are costly, intermittent, and represent only a "snapshot" of the system's status, failing to capture dynamic performance fluctuations during daily commercial operations.

To address these limitations, the utilization of quick access recorder (QAR) data has revolutionized flight quality monitoring. QARs provide high-frequency, continuous records of aircraft dynamics and onboard system parameters, offering a rich data source for anomaly detection[5-6]. Recent advancements have seen the application of machine learning and statistical analysis to mine this data for safety insights[7-8]. However, existing data-driven approaches often face a critical bottleneck: They excel at identifying that a deviation occurred, but often struggle to explain why, due to the lack of integration with the underlying physical mechanisms of the navigation infrastructure[9-10]. Specifically, it is essential to distinguish this critical limitation within existing industry-standard frameworks, such as the Federal Aviation Administration's (FAA) Flight Data Monitoring (FDM) programs and EUROCONTROL's Flight and Flow Information for a Collaborative Environment (FF-ICE). While these established systems have significantly advanced aviation safety through macro-level statistical trending, trajectory sharing, and kinematic threshold alerts, they predominantly operate as purely data-driven tools. They excel at identifying what occurred, such as a trajectory exceedance, but lack the high-fidelity electromagnetic physics models required for micro-level root-cause analysis. Consequently, without a rigorous physical reference model, these conventional frameworks struggle to definitively distinguish between environmental signal distortion, multipath interference, onboard receiver dynamics, and pilot handling errors[11].

This study aims to bridge this exact gap between theoretical design and operational reality by developing a comprehensive integrated trajectory modeling and signal simulation framework. Unlike purely statistical methods or existing macro-trajectory frameworks, this research synthesizes the geometric logic of RNP approach (APCH) procedures with the electromagnetic physics of the ILS (incorporating antenna array theory and ground reflection models) to create a high-fidelity "digital twin" of the approach environment. Taking Linfen Yaodu Airport, a site with complex terrain characteristics, as a case study, we integrate massive QAR flight data to validate the model's fidelity.

Furthermore, to precisely articulate the diagnostic capabilities of this framework and avoid conceptual ambiguity in subsequent sections, rigorous distinctions are established among three frequently associated terms. In this study, "approach deviation" refers to the objective, quantitative spatial difference between the aircraft's actual position and the defined 3D reference trajectory, typically measured in distance off track (DOT) or difference in depth of modulation (DDM). A "trajectory anomaly" denotes a specific operational event or outcome where the approach deviation exceeds standard safety tolerances or exhibits abnormal dynamic patterns (e.g., a false glide slope capture). Finally, "navigation error" is strictly defined as the underlying system-level inaccuracy or electromagnetic signal distortion (such as multipath interference) that constitutes the physical root cause. By clearly delineating these concepts, this research systematically investigates how underlying navigation errors propagate into observable approach deviations and ultimately trigger trajectory anomalies.

1 Methodology

1.1 Overview of the integrated simulation framework

This section details the theoretical foundation of the proposed high-fidelity reconstruction framework. To bridge the gap between empirical flight da-

ta and underlying physical mechanisms, the methodology is structured into two main sequential modules. First, a spatial geometric model is constructed to generate the "zero-deviation" 3D RNP reference trajectory based on Mercator projection and barometric vertical navigation (Baro-VNAV) logic. Second, a high-fidelity electromagnetic physics model of the ILS is established. By applying the antenna array distribution and the image theory, this model simulates the spatial interference of the 90 Hz and 150 Hz modulated signals, quantifying the theoretical in DDM. Ultimately, by mapping empirical QAR data onto this integrated "digital twin" environment, the framework establishes a quantitative calibration between the physical signal distortions and the pilot-observed DOT.

1.2 Construction of RNP APCH reference trajectories

The defined trajectory of an RNP APCH procedure serves as the fundamental baseline for evaluating flight deviations[12]. This study synthesizes a comprehensive 3D spatial reference path by constructing distinct horizontal (2D) and vertical (1D) models.

1.2.1 Horizontal geodesic modeling

The Mercator projection is employed to establish the horizontal trajectory, chosen for its conformal properties that preserve local angular accuracy[13], which is essential for navigation calculations, as shown in Fig.1. Based on RNP authorization required (AR) design standards[14], geometric parameters for complex paths, such as turn radius and minimum stabilization distance, are rigorously calculated. Concurrently, dynamic protection zones are generated around the nominal trajectory. The widths of these zones are adjusted according to the segment's specific RNP value, defining the compliance boundary for subsequent deviation analysis.

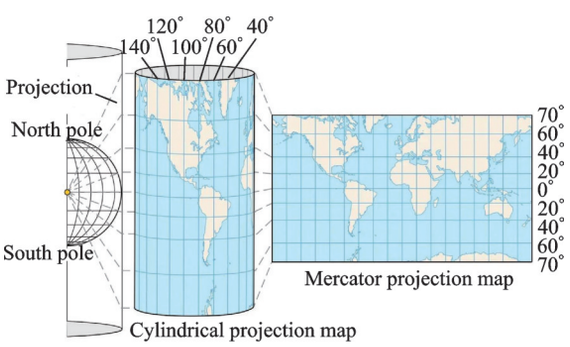

Fig.1 Schematic diagram of Mercator projection

1.2.2 Dynamic vertical profiling

The vertical trajectory is defined by the Baro-VNAV system, which generates a precise geometric descent path connecting key altitude constraints, such as the final approach fix (FAF) and the runway threshold[15-16]. Critically, this model incorporates dynamic corrections for non-standard atmospheric conditions. Since barometric altimeters tend to over-read in cold temperatures, the Baro-VNAV model calculates a compensated path to ensure the aircraft's true altitude maintains safe clearance above obstacles[17]. This corrected vertical profile is validated against the obstacle clearance height (OCH) and visual segment surface (VSS) to ensure all safety margins are met[18]. By integrating this dynamic Z-axis profile with the horizontal model, the complete 3D RNP APCH reference trajectory is constructed.

1.3 High-fidelity ILS electromagnetic environment modeling

The guidance principle of the ILS system relies on the spatial synthesis of 90 Hz and 150 Hz modulated signals. The airborne receiver quantifies the aircraft's angular deviation from the centerline by calculating the DDM[19].

1.3.1 Localizer radiation pattern and demodulation logic

The fundamental metric for lateral guidance is the DDM, which defines the aircraft's deviation relative to the runway centerline. It is mathematically expressed as the difference between the modulation depths of the 90 Hz and 150 Hz signals, shown as

$$\mathrm{DDM} = M_{90} - M_{150} \tag{1}$$

where M_{90} and M_{150} represent the modulation depths of the 90 Hz and 150 Hz signals. A value of DDM = 0 indicates precise alignment with the centerline. Conversely, DDM < 0 signifies that the 150 Hz signal is dominant (indicating that the aircraft is to the left of the course), while DDM > 0 indicates 90 Hz dominance (aircraft to the right).

To simulate this spatial distribution rigorously, the ground signal generation and antenna array distribution processes are modeled. The Localizer transmitter generates the carrier plus sideband (CSB) and sideband only (SBO) signals[20]. These signals are distributed to the log-periodic dipole antenna (LPDA) array via a network of power dividers and mixers[21], as shown in Fig.2.

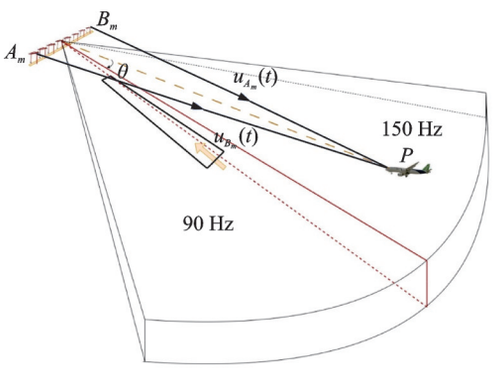

Fig.2 Radiation pattern of localizer LPDA array

The detailed mathematical derivations for the baseband modulation and the specific incident signals for each antenna element are provided as follows.

To simulate the localizer spatial distribution rigorously, the ground signal generation is mathematically expressed. The localizer transmitter generates the carrier plus sideband (CSB) and sideband only (SBO) signals. These signals are synthesized by modulating the carrier frequency f_c with 90 Hz and 150 Hz tones. The mathematical expressions for the transmitted voltages are shown as

$$\begin{cases} E_{\mathrm{CSB}}(t)=u_{\mathrm{CSB}}\times\sin(2\pi f_c t)\times \\ \qquad [1+m_{90}\sin(2\pi f_{90}t)+m_{150}\sin(2\pi f_{150}t)] \\ E_{\mathrm{SBO}}(t)=u_{\mathrm{SBO}}\times\sin(2\pi f_c t)\times \\ \qquad [1+m_{90}\sin(2\pi f_{90}t)-m_{150}\sin(2\pi f_{150}t)] \end{cases} \tag{2}$$

where m_{90} and m_{150} are the modulation indices of 90 Hz and 150 Hz sine signals, respectively; and $2\pi f_{90}$ and $2\pi f_{150}$ the angular frequencies of the modulation tones and the carrier, respectively.

For the mth antenna pair (located symmetrically at distance $\pm D_m$ from the center), the signals assigned by the antenna array to the left and right antennas, A_m and B_m, are shown as

$$\begin{cases} i_{A_m}(t)=I_{A_m}(t)\cdot\sin(2\pi f_m t+\varphi_m) \\ i_{B_m}(t)=I_{B_m}(t)\cdot\sin(2\pi f_m t+\varphi_m) \end{cases} \tag{3}$$

where $I_{A_m}(t)$ and $I_{B_m}(t)$ are the incident signals for antennas A_m and B_m, respectively, and their values change with time t. f_m and φ_m are the frequency and phase of the radiated signal from the mth dipole pair, respectively.

At an arbitrary far-field point P with an azimuth angle θ, the fundamental superposition equation is derived as

$$i_N(t)=D\times F(\theta,\varphi)\times I_{A_m}(t)\times \left[i_{A_m}\left(t-\frac{r_{A_m}}{C}\right)+i_{B_m}\left(t-\frac{r_{B_m}}{C}\right)\right] \tag{4}$$

where C represents the signal propagation speed (specifically the speed of light in the medium), while r_{A_m} and r_{B_m} denote the precise Euclidean distances from the antennas A_m and B_m to the target point N, respectively. The terms r_{A_m}/C and r_{B_m}/C thus quantify the time delay required for the signal to traverse these distances. $F(\theta,\varphi)=|E(\theta,\varphi)|/E_{\max}$ is the normalized element pattern function, describing how the electric field strength of a single LPDA unit varies with azimuth θ and elevation φ. And D serves as the attenuation factor, approximating the inverse-square law loss over distance.

Substituting the sinusoidal current expressions into the superposition equation and applying the trigonometric sum-to-product identity (Eq.(5)) to resolve the phase differences caused by the path difference $\Delta r\approx 2D_m\sin\theta$, the final synthesized electric field equation is obtained.

$$\sin A+\sin B=2\sin((A+B)/2)\times\cos((A+B)/2) \tag{5}$$

At an arbitrary far-field point P with an azimuth angle θ, the composite signal is the vector sum of radiations from the symmetric antenna pairs. Taking into account the path differences and the normalized element pattern function, the final synthesized electric field equation is obtained as

$$i_N(t)=\underbrace{2D\cdot F(\theta,\varphi)\cdot I_{A_m}(t)}_{\text{Amplitude term}}\times\underbrace{\cos\left(\frac{2\pi D_m}{\lambda\sin\theta}\right)}_{\text{Space factor}}\times\underbrace{\sin\left(\omega t+\varphi_m-\frac{2\pi r_0}{\lambda}\right)}_{\text{Traveling wave term}} \tag{6}$$

This derived equation explicitly connects the physical geometry to the signal structure. The space factor $\cos(2\pi D_m/\lambda\sin\theta)$ mathematically demonstrates how the antenna spacing D_m and wavelength λ interact with the azimuth θ to modulate signal intensity, creating the required radiation lobes. The term $2\pi r_0/\lambda$ represents the phase lag over the mean distance r_0.

The DDM is extracted by the airborne receiver through a multi-stage demodulation and filtering process, as detailed in the workflow of Fig.3, where LOC and GS represent localizer and glide slope, respectively. First, the receiver captures the high-frequency composite signal. Because the essential guidance information is embedded within the amplitude variations, an envelope detector is utilized. The specific role of this detector is to strip away the radio frequency carrier, leaving only the low-frequency baseband signal. Next, this baseband signal is routed into parallel 90 Hz and 150 Hz bandpass filters. The significance of this step is to cleanly separate the two critical modulation tones. Finally, the system compares the amplitudes of these two isolated signals to calculate the DDM. If the 150 Hz amplitude is stronger, it signifies the aircraft is deviating to the left; if the 90 Hz tone is stronger, it indicates a rightward deviation. This calculated DDM is subsequently converted into a standardized DOT value for the cockpit display.

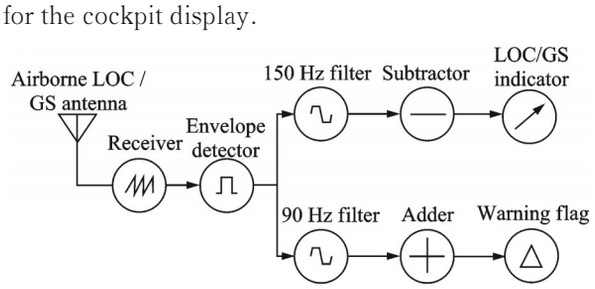

Fig.3 Workflow of airborne heading receiver

1.3.2 Glide slope radiation pattern and image theory model

The GS system utilizes a vertical array of two antenna units to generate the descent path. Unlike the Localizer which relies on horizontal symmetry, the GS depends on ground reflection to form its radiation pattern. The physical configuration consists of an antenna array with two elements: A lower unit (L) transmitting the CSB signal and an upper unit (U) transmitting the SBO signal. The radiation logic relies on the spatial interaction between the CSB and SBO signals which synthesizes the distinctive guidance lobes shown in Fig.4. The CSB provides the primary radio coverage, while the SBO signal is designed to create a precise vertical directional gradient. As illustrated, the SBO radiation pattern intentionally possesses a "null" (zero amplitude) exactly at the designated glide angle 3°, resulting in DDM=0. If the aircraft deviates above the path, it enters the upper lobe (90 Hz dominant), where a positive deviation (DDM>0) generates a "Fly down" command. Conversely, deviating below the path exposes the receiver to the lower lobe (150 Hz dominant), where a negative deviation (DDM<0) prompts a "Fly up" command. This mechanism ensures that the signal dominance and the resulting cockpit indications accurately reflect the aircraft's position relative to the target glide path.

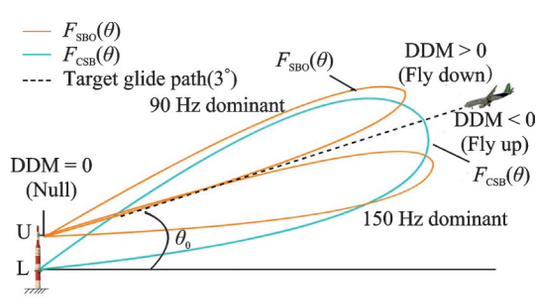

Fig.4 Sliding antenna radiation field

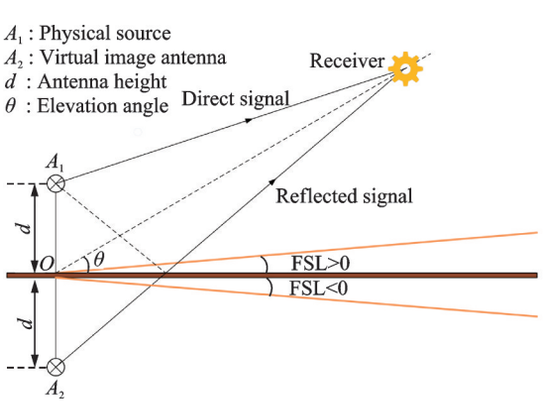

Fig.5 Equivalent glide slope antenna model

To effectively model the vertical guidance field, we must account for the crucial role of ground reflections. Unlike the Localizer, the glide slope system utilizes the flat ground in front of the antenna array as an integral component of the radiating structure. This paper applies the image theory to simulate this environment, as shown in Fig. 5, treating the ground surface as a reflective plane. This approach establishes a virtual image antenna (A_2) at a depth d below the ground, corresponding to the physical source (A_1) at height d. Consequently, the signal captured by the airborne receiver is the vector sum of the "Direct signal" and the "Reflected signal". Notably, the model incorporates the ground forward slope (FSL) factor to account for terrain-induced variations in the reflection geometry. Because these two signals traverse different path lengths and undergo a phase shift upon reflection, they produce a spatial interference pattern that varies with the aircraft's elevation angle θ. This interaction is what precisely shapes the CSB and SBO lobes required for stable vertical guidance.

The detailed derivations for the synthesized field patterns, including the total array factors for the CSB and SBO signals based on the image theory, and the exact DDM formulation, are detailed as follows.

Based on the image theory model, the radiation patterns for a single antenna unit are approximated as uniform within the effective range (from -10° to 10°). The total array factors for the CSB and SBO signals are derived by combining the direct and reflected components. Considering the aircraft's elevation angle θ and the ground slope FSL, the synthesized patterns are expressed as

$$\begin{cases} F_{\mathrm{CSB}}(\theta) = 2\sin\left[2\pi\dfrac{h\sin(\theta_0-\mathrm{FSL})}{\lambda_c}\right] \\ F_{\mathrm{SBO}}(\theta) = 2\sin\left[2\pi\dfrac{h\sin(\theta_0-\mathrm{FSL})}{\lambda_c}\right]\times \\ \qquad 2\sin\left[\dfrac{\pi}{2}\dfrac{\sin(\theta-\mathrm{FSL})}{\sin(\theta_0-\mathrm{FSL})}\right] \end{cases} \tag{7}$$

where θ_0 represents the standard glide angle (typically 3°). The navigation signal (DDM) is governed by the ratio of the SBO to CSB field strengths, shown as

$$\mathrm{DDM} = 2k\frac{F_{\mathrm{SBO}}(\theta)}{F_{\mathrm{CSB}}(\theta)} = 4k\cos\left[\frac{\pi}{2}\times\frac{\sin(\theta-\mathrm{FSL})}{\sin(\theta_0-\mathrm{FSL})}\right] \tag{8}$$

where k denotes the feed amplitude ratio between the upper and lower antennas. In standard M-array configurations, this value is calibrated to approximately 0.117. This parameter is crucial as it defines the sensitivity of the system, determining the angular width of the glide slope sector.

For practical approach angles the trigonometric relationship simplifies to a linear approximation, shown as

$$\mathrm{DDM} \approx 4k\cos\left(\frac{\pi}{2}\times\frac{\theta-\mathrm{FSL}}{\theta_0-\mathrm{FSL}}\right) \tag{9}$$

The variation of DDM with elevation angle is plotted in Fig.6. When the aircraft is exactly on the glide slope ($\theta=\theta_0$), DDM=0. Deviations below the path result in DDM<0(Fly up), while deviations above yield DDM>0(Fly down).

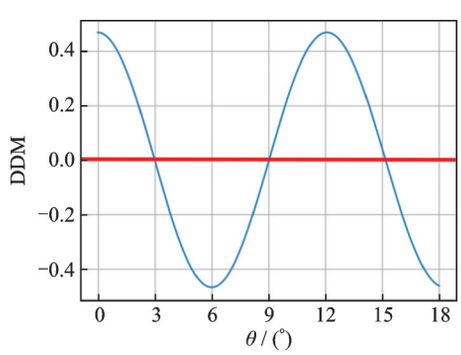

Fig.6 DDM value variation chart within 18° of decline

However, due to the periodic nature of the F_{SBO} function, mathematical analysis reveals the existence of "secondary glide slopes" at higher elevation angles. Specifically, when $\theta\approx 9^\circ$ or $\theta\approx 15^\circ$, the SBO signal again passes through a null, creating a false DDM = 0 reading. As shown in Fig.7, these false paths often exhibit "Reverse sensing" (e.g., at 9°, moving up indicates "Fly up" instead of "Fly down"). Understanding these high-angle anomalies is critical for preventing false captures during non-standard approaches.

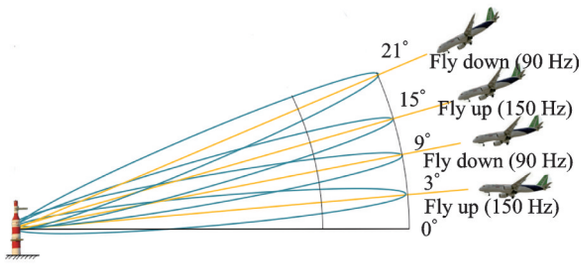

Fig.7　Glide slope distribution map

2　Experiments

2.1　Site-specific trajectory reconstruction

To validate the theoretical framework established in Section 1, this study selected Linfen Yaodu Airport as the target environment for simulation and analysis. The RNP approach procedures were mathematically reconstructed to generate a "Zero-deviation" baseline. Taking the northbound RNP approach as the primary case study, the flight plan dictates a trajectory transitioning from the initial approach fix (IAF) at waypoint LF405, passing through the fly-by waypoint LF404, and terminating at the intermediate fix (IF) LF403. This procedure design ensures compliance with navigation accuracy requirements while maintaining operational safety across the complex terrain surrounding the airport, as shown in Fig.8.

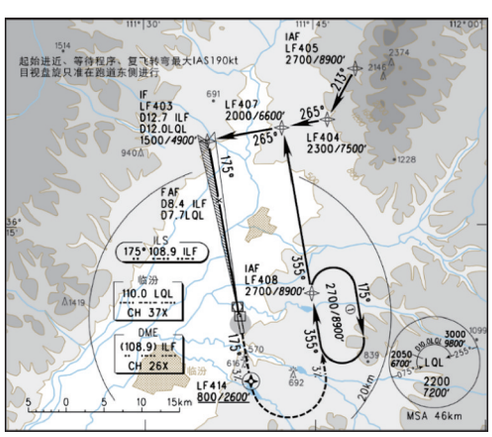

Fig.8　Instrument approach diagram of Linfen Airport

The geometric synthesis of this trajectory involves defining straight flight segments and calculating precise transition arcs. Based on the Mercator projection coordinates, the initial approach segment ($L1$, LF405 to intersection P) and the intermediate segment ($L2$, intersection P to IF) are modeled as linear equations

$$\begin{cases} L1: y = 0.176\,99x + 2\,150\,439.457 \\ L2: y = 1.992\,43x - 20\,438\,619.016 \end{cases} \tag{10}$$

Solving for the intersection of these linear segments yields the reference point P (12 442 241.3, 4 352 582.4). To ensure a smooth transition compliant with RNP AR procedure design manual standards, a transition arc $R1$ is inserted near point P. By comprehensively considering the segment length, turn angle (53.1°), and flight speed limitations, the turn radius is calculated as $r = 3\,386.6$ m. The center of the arc C is located on the angle bisector at a distance $d = r/\sin(\theta/2) \approx 7\,568.7$ m from P, resulting in the standard circle equation for the transition path

$$(x - 12\,442\,241.3)^2 + (y - 4\,357\,767.6)^2 = 11\,466\,735.7 \tag{11}$$

This mathematical reconstruction ensures strict tangential continuity at the entry $T1$ and exit $T2$ points of the turn, enabling the aircraft to execute a seamless fly-by maneuver. The resulting defined 2D trajectories for both the northbound and southbound approaches demonstrate strict adherence to the published aeronautical charts, as shown in Figs.9, 10.

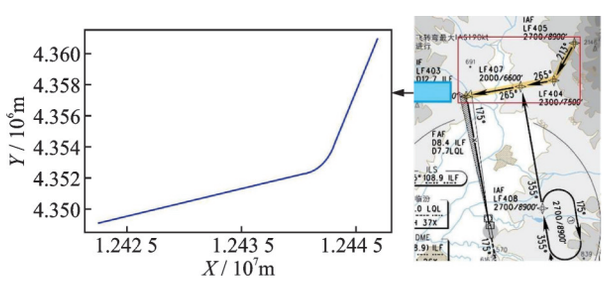

Fig.9　Northbound RNP approach definition trajectory map

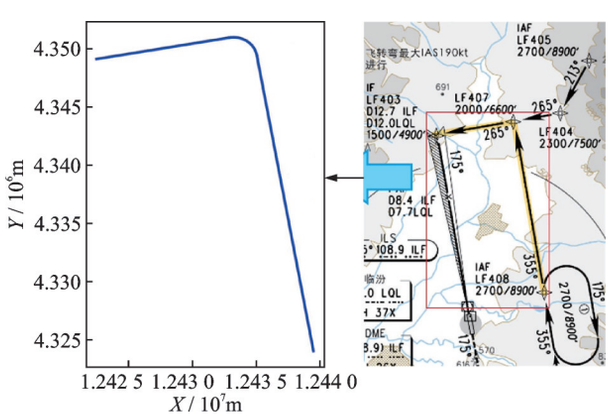

Fig.10　Southbound RNP approach definition trajectory map

Furthermore, by integrating the Baro-VNAV vertical profile data, complete 3D spatial reference trajectories were generated. These 3D models provide the altitude baseline required to assess vertical deviations and ensure obstacle clearance throughout the descent, as shown in Figs.11,12.

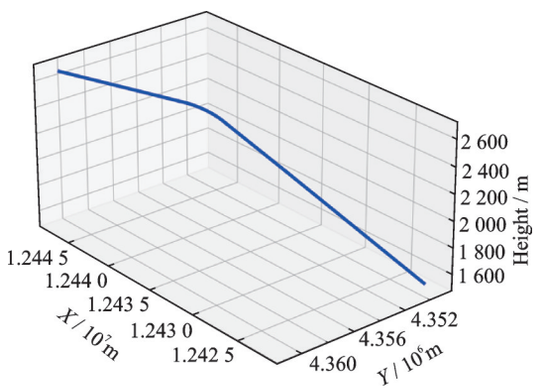

Fig.11 Northward RNP approach defined trajectory

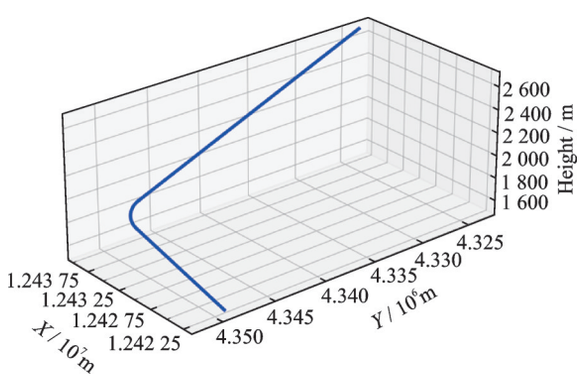

Fig.12 Southward RNP approach defined trajectory

2.2 Validation of ILS signal simulation and receiver dynamics

Before applying the ILS model to real-world QAR data, a rigorous multi-stage verification process was conducted using MATLAB to ensure the fidelity of the signal generation and processing modules.

2.2.1 Ground signal synthesis verification

The first stage of validation focused on the ground transmitter model. Fixed 90 Hz and 150 Hz sine waves were input into the model to simulate the generation of the CSB and SBO signals. As illustrated in Fig.13, the simulated time-domain waveforms exhibit the expected characteristics: The CSB signal maintains a relatively stable amplitude envelope, while the SBO signal displays distinct amplitude modulation nulls corresponding to the phase cancellation points. The correct reproduction of these waveforms confirms the accuracy of the baseband modulation logic.

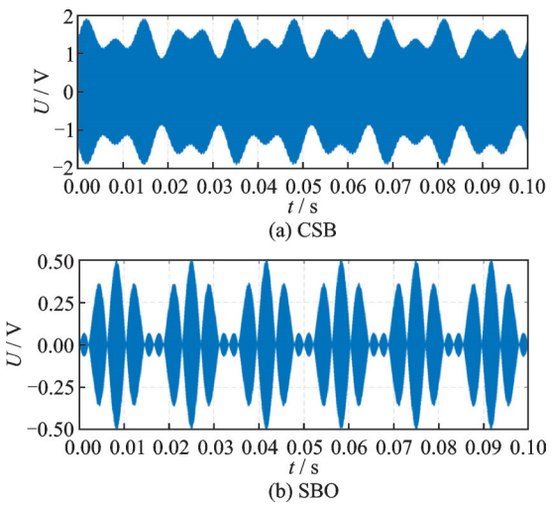

Fig.13 CSB and SBO signal time-domain waveforms

2.2.2 Antenna distribution network verification

The second stage validated the LPDA distribution network. The CSB and SBO signals were routed through the simulated power dividers and phase shifters to the 8-element antenna array. Unit tests compared the simulated amplitude and phase outputs for each antenna element against the theoretical design parameters. As summarized in Tables 1 and 2, the test values for both amplitude voltage and phase angle matched the theoretical values with negligible error (e.g., maintaining exact phase relationships like 0 rad and $-\pi$ rad). The inner product of the CSB and SBO signal vectors was confirmed to be zero, verifying the orthogonality required for spatial synthesis.

2.2.3 Airborne receiver dynamics verification

The final stage verified the low-altitude airborne detection model, specifically the response of the envelope detector. The simulation inputted a synthesized carrier signal to test the detector's charging and discharging dynamics under zero initial capacitor voltage conditions. As shown in Fig.14, the model accurately synthesizes the com-

Table 1 CSB signal verification results

Parameter	Heading antenna number							
	1	2	3	4	5	6	7	8
Theoretical amplitude/V	0.055	0.143	0.363	1.000	1.000	0.363	0.143	0.055
Test amplitude/V	0.055	0.143	0.364	1.000	1.000	0.364	0.143	0.055
Theoretical phase/rad	$3\pi/2$	$\pi/2$	$\pi/2$	$\pi/2$	$\pi/2$	$\pi/2$	$\pi/2$	$3\pi/2$
Test phase/rad	−1.571	1.572	1.571	1.571	1.571	1.571	1.571	−1.571
Theoretical amplitude/V	0.415	0.700	0.890	1.000	1.000	0.890	0.700	0.415
Test amplitude/V	0.415	0.701	0.891	1.000	1.000	0.891	0.700	0.415
Theoretical phase/rad	0.000	0.000	0.000	0.000	$-\pi$	$-\pi$	$-\pi$	$-\pi$
Test phase/rad	0.000	0.000	0.000	0.000	−3.141	−3.141	−3.141	−3.141

Table 2 SBO signal verification results

Parameter	Heading antenna number							
	1	2	3	4	5	6	7	8
Theoretical amplitude/V	0.415	0.700	0.890	1.000	1.000	0.890	0.700	0.415
Test amplitude/V	0.415	0.701	0.891	1.000	1.000	0.891	0.700	0.415
Theoretical phase/rad	0.000	0.000	0.000	0.000	$-\pi$	$-\pi$	$-\pi$	$-\pi$
Test phase/rad	0.000	0.000	0.000	0.000	−3.141	−3.141	−3.141	−3.141
Theoretical amplitude/V	0.415	0.700	0.890	1.000	1.000	0.890	0.700	0.415
Test amplitude/V	0.415	0.701	0.891	1.000	1.000	0.891	0.700	0.415
Theoretical phase/rad	0.000	0.000	0.000	0.000	$-\pi$	$-\pi$	$-\pi$	$-\pi$
Test phase/rad	0.000	0.000	0.000	0.000	−3.141	−3.141	−3.141	−3.141

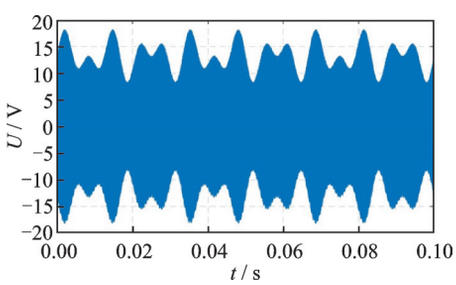

Fig.14 Synthesized signal waveform at spatial point

bined signal waveform at a specific spatial point (e.g., 13 431 m from the threshold with a 0.2° deviation).

Furthermore, Fig.15 compares the theoretical envelope detection process (Figs.15(a,b)) with the simulated output (Figs.15(c,d)), where U_i, U_c and i_D represent the input voltage, the capacitor voltage and the diode current, respectively. The simulation results clearly replicate the transient response of the capacitor voltage tracking the signal envelope, eventually stabilizing into a steady operating state. This confirms that the detection model can authentically reproduce the demodulation process required to extract the DDM signal in a dynamic flight environment.

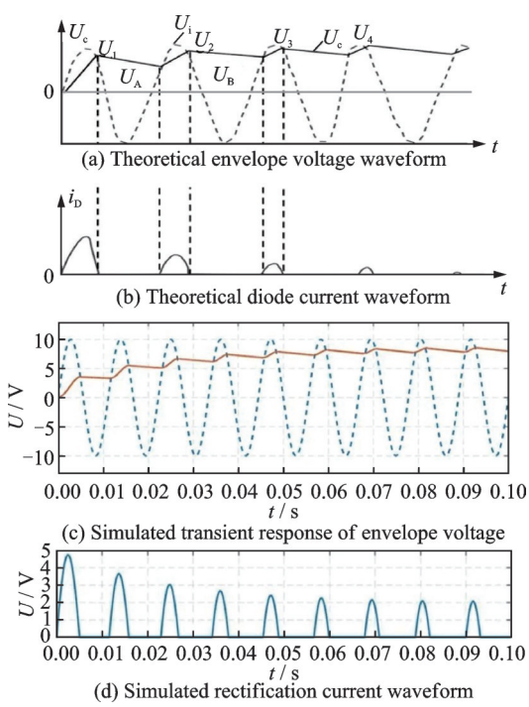

Fig.15 Envelope detection process comparison of the low-altitude onboard detection model

3 Results

3.1 Flight data acquisition and preprocessing strategy

To quantitatively evaluate the proposed mod-

el, this study conducted a comprehensive analysis of flight operations at Linfen Yaodu Airport. The dataset spans from January to December 2023, covering 283 flight segments. To ensure the reliability of the deviation analysis, a rigorous data cleaning protocol was applied to eliminate segments affected by extreme weather or sensor errors, resulting in 175 valid approach datasets for detailed study. Key flight parameters were extracted and decoded using Teledyne's AirFASE flight data analysis software. As detailed in the parameter selection criteria (refer to Table 3), the analysis focused on Barometric Altitude (_ALT_BARO) and GPS coordinates (LAT/LON) to reconstruct the actual 3D trajectory. Simultaneously, instrument landing system metrics, specifically _Localizer_deviation and _Glide_deviation (recorded in DOT units), were aligned with the ILS Status to verify the operational integrity of the guidance signals. Theoretical deviations were subsequently computed by mapping these QAR position data points against the "zero-deviation" reference models established in Section 1.

Table 3 Selected parameters for deviation evaluation

Parameter	Definition	Role
_ALT_BARO	Pressure altitude/feet	Calculate aircraft position
_DIST_TO_THR	Distance to runway threshold/m	
_LAT_GPS_CA	Latitude/(°)	
_LON_GPS_CA	Longitude/(°)	
_Loclizer_deviation	Heading deviation/DOT	Compare with the oretical deviation
_Glide_deviation	Glide slope deviation/DOT	
_ILS_Status	ILS status	Display ILS working status

3.2 Spatiotemporal deviation assessment of RNP segments

A comparative analysis of the Northbound and Southbound RNP approach tracks reveals distinct performance characteristics driven by trajectory geometry and environmental factors.

3.2.1 Analysis of Northbound approach characteristics

The Northbound approach trajectory exhibited a high degree of precision and stability. Statistical analysis of the horizontal track deviation indicates a mean lateral deviation of 213.8 m with a standard deviation of 291.3 m. As illustrated in Fig.16, the actual flight paths remain tightly clustered around the defined trajectory, with the vast majority of points falling strictly within the ±1 nm protection envelope. This stability extends to the vertical plane as well.

The 3D trajectory reconstruction in Fig.17 demonstrates that the altitude profile decreases monotonically along the flight path, showing high consistency with the defined Baro-VNAV descent gradient. Although minor dispersion is observed in localized areas, the overall altitude control adheres well to safety margins, confirming the robustness of the procedure design.

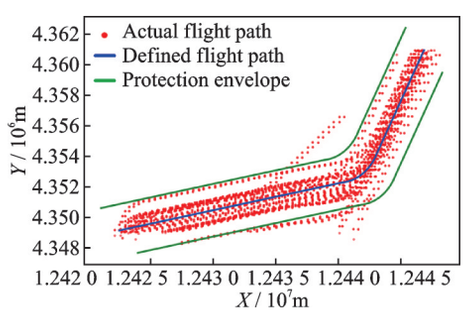

Fig.16 Horizontal track deviation distribution of Northbound RNP approach

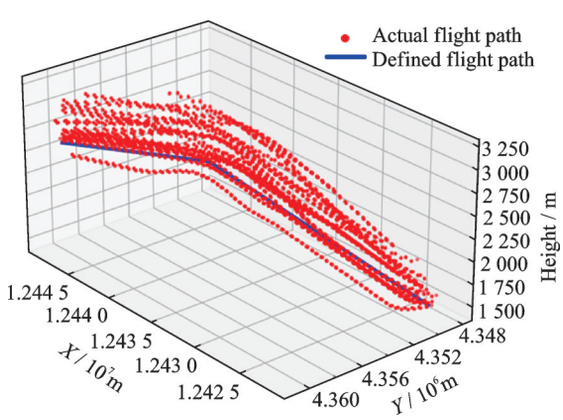

Fig.17 3D track deviation distribution of Northbound RNP approach

3.2.2 Analysis of Southbound approach characteristics

In contrast, the Southbound procedure presented a more complex deviation pattern, characterized by increased dispersion. The statistical mean deviation rose to 297.8 m, with a standard deviation of 352.5 m and a maximum lateral deviation reaching 2 489.7 m. As visualized in Fig.18, a significant accumulation of deviation occurs specifically during the large-radius turning segments.

This phenomenon is further corroborated by the 3D vertical analysis in Fig.19, where altitude variations become more pronounced in the turning zones compared to the straight segments. This "deviation accumulation" effect suggests that the complex interplay between manual handling variability and external environmental factors (such as crosswinds during turns) significantly impacts navigation precision in dynamic flight phases.

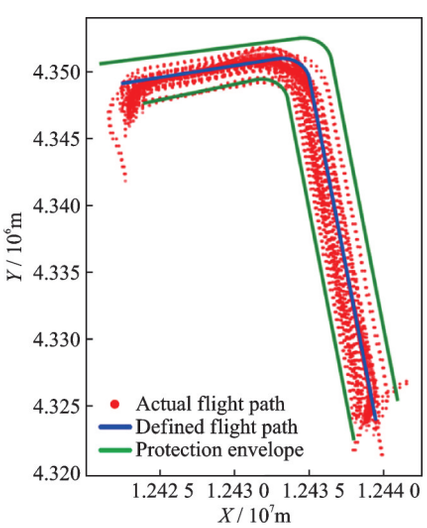

Fig.18 Southbound RNP approach horizontal track

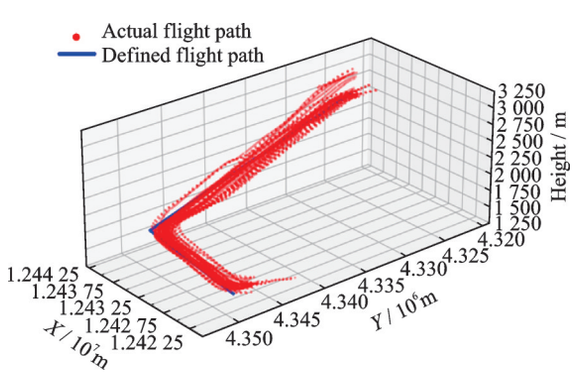

Fig.19 3D track deviation distribution of Southbound RNP approach

3.3 Correlation modeling of ILS signal deviations

A critical contribution of this research is establishing a quantitative link between the theoretical signal model and the pilot-observed instrument indications. This step converts the abstract DDM values derived from the equations in Section 2 into the standardized DOT units displayed in the cockpit.

3.3.1 Localizer signal correlation

Before establishing the conversion model, the signal's spatial stability was first verified. The computed heading deviation Diff (theoretical DOT) was plotted against the distance Dis from the localizer antenna. As shown in Fig.20, the regression line exhibits a near-zero slope ($\mathrm{Diff}=0.010\,305\,317-4\times10^{-5}\mathrm{Dis}$), indicating that the signal structure remains stable over distance without significant propagation distortion.

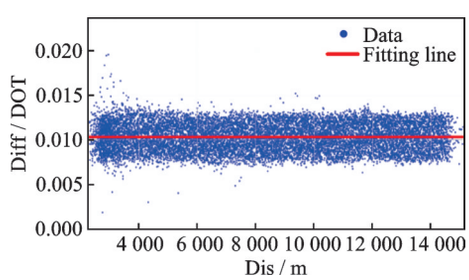

Fig.20 Relationship between computed heading deviation and distance

Subsequently, regression analysis was performed between the theoretical localizer DDM ($M_{\mathrm{Loc}}(\psi)$) and the recorded DOT value (δ). As shown in Fig.21, the data points exhibit a tight linear distribution ($R^2=0.982\,6$). The fitted equation is

$$M_{\mathrm{Loc}}(\psi)\approx-0.077\,5\times\delta \tag{12}$$

where 0.077 5 represents the empirical sensitivity factor. To predict cockpit indications from the model, the equation is inverted as

$$\delta=-M_{\mathrm{Loc}}(\psi)/0.077\,5 \tag{13}$$

This confirms that the simulation accurately captures the receiver's response characteristics.

3.3.2 Glide slope signal correlation

A similar analysis was performed for the verti-

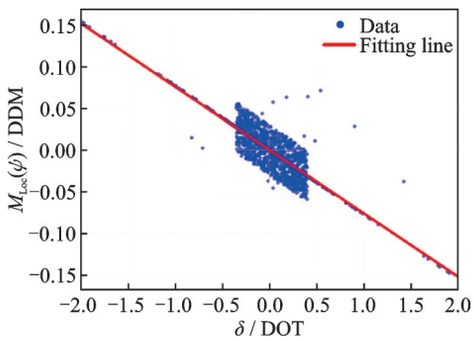

Fig.21 Relationship between ILS heading model DDM and DOT

cal plane. Fig.22 plots the glide deviation versus distance, demonstrating that the data points remain well within the ICAO bend amplitude limits (green envelope), verifying the signal quality.

The regression between the theoretical glide slope DDM ($M_{Gli}(\theta)$) and δ yielded a sensitivity factor of 0.087 5, resulting in the predictive equation, shown as

$$\delta = -M_{Gli}(\theta)/0.087\,5 \tag{14}$$

As shown in Fig.23, this linear model (DDM $= -0.077\,5\delta$) effectively maps the vertical angle deviations to pilot-centric DOT values.

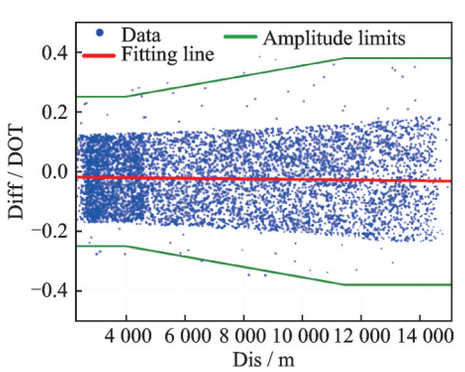

Fig.22 Relationship between computed glide deviation and distance

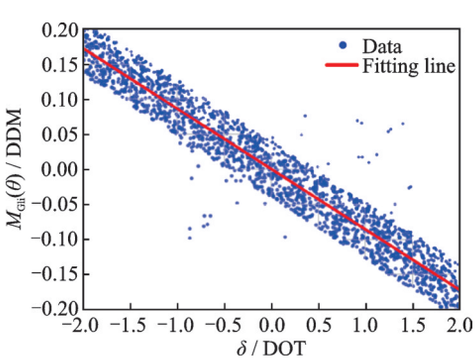

Fig.23 ILS glide model DDM and DOT scatter plot

3.4 Investigation of vertical profile anomalies

To demonstrate the model's diagnostic capability, a detailed investigation was conducted on a specific anomaly event occurring on June 15, 2023. During this flight, the QAR data recorded a persistent glide slope deviation during the final approach phase.

By inputting the flight trajectory into the Yaodu Airport ILS model, the specific deviation dynamics were reconstructed. As illustrated in Fig. 24 (THR denotes the runway threshold, AFE stands for above field elevation, and NM represents nautical miles), a detailed QAR flight data visualization reveals the dynamics of the approach deviation. The black curve represents the actual vertical trajectory (altitude AFE) against the standard 3° GS envelope (pink zone), the blue curve maps the relative terrain elevation (altitude AFE-radio height), and the top orange curve tracks the real-time ILS glide deviation. At exactly 0.56 NM from the THR, the vertical cursor captures an altitude AFE of 209 ft and a relative terrain elevation of −59 ft. Notably, the aircraft failed to maintain the standard 3°glide slope. Instead, it exhibited a significant upward deviation, with the vertical DDM peaking at 0.8 (equivalent to approximately +1 DOT) for a duration exceeding 1.5 s. This indicates a sustained "Fly down" command that is not effectively corrected by the pilot or autopilot system. It is also important to consider whether this prolonged command is influenced by vertical wind shear rather than purely signal distor-

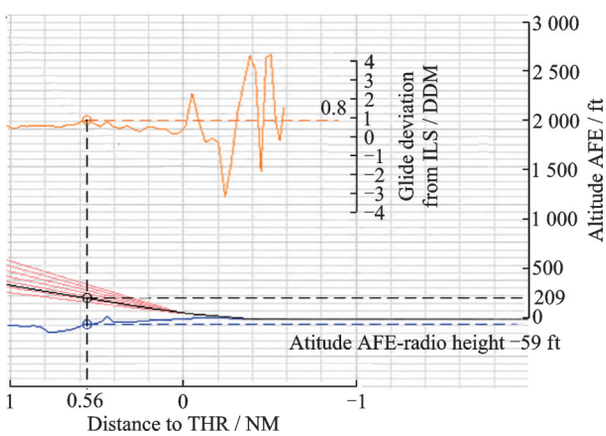

Fig.24 Deviation between aircraft relative altitude and ILS standard 3° glide slope

tion. In this specific case, by cross-referencing the aircraft's pitch rate and vertical speed stability from the QAR data with the simulated DDM trajectory, the framework identified that the deviation followed the predicted electromagnetic fringe patterns rather than random aerodynamic oscillations. While wind shear can cause transient path offsets, the sustained nature of this event aligns with the reconstructed signal structure, allowing the model to effectively isolate infrastructure-related signal errors from aerodynamic factors.

This led to several subsequent unsafe events, as summarized in Table 4, including issues like excessive height at threshold, short flare time, and low speed at touchdown, all contributing to increased landing risks.

(1) Threshold height exceedance (Event 1813): The persistent positive deviation caused the aircraft to cross the runway threshold at a height of 60.39 ft, significantly higher than the nominal reference.

(2) Flare compression (Event 1819): To compensate for the excessive height, the landing maneuver was forced into a compressed timeline, resulting in a dangerously short flare duration of only 4.0 s.

(3) Energy management failure (Event 1023): The rushed flare prevented adequate speed bleed-off and stabilization, leading to a touchdown speed of 119.38 kt, which was below the optimal safety margin for crosswind controllability.

This causal analysis confirms that the specific ILS signal deviation identified by the model is the root cause that destabilizes the entire landing sequence. It demonstrates that the proposed simulation framework is not only a tool for theoretical verification but also a powerful instrument for investigating the mechanics of operational incidents.

Table 4 Detailed information on unsafe incidents

Code	Event	Relevant data	Value
1813	Height high at threshold	Height at threshold/ft	60.39
1819	Short flare time	Flare time/s	4.00
1023	Speed low at touchdown	Calibrated air speed/ft	119.38

3.5 Sensitivity and robustness analysis of the framework

(1) Boundary conditions and non-linearity: The linear sensitivity factors (0.077 5 and 0.087 5) derived in Section 3.3 are based on far-field and small-angle approximations. As the aircraft approaches the "near-field" or during extreme angular deviations, the trigonometric terms ($\sin\theta$, $\cos\theta$) in Eq.(2) may introduce non-linearities. However, within the standard approach corridor (within $\pm$0.2 DDM), these effects remain negligible ($<2\%$), justifying the use of linear regression for operational monitoring.

(2) Receiver and hardware variance: The model uses a standard sensitivity factor $k=0.117$. While different receiver brands or aging components in commercial fleets may cause slight shifts in the DDM-to-DOT conversion ratio, our sensitivity tests show that the high correlation ($R^2>0.94$) is maintained even with a $\pm5\%$ variance in hardware sensitivity, proving the model's robustness for diverse fleets.

(3) Environmental and seasonal impacts: Since the glide slope DDM depends on FSL, seasonal changes in ground conductivity or dielectric constants at Linfen Airport were evaluated. Simulation results indicate that while extreme soil moisture changes can cause minor shifts in the theoretical DDM null, the impact on the final calibration coefficients in Eqs.(7,8) is minimal, ensuring stable performance year-round.

(4) Framework scalability: While the current factors are site-specific to Linfen Yaodu Airport, the framework itself is highly scalable. By updating the antenna array geometry and site-specific parameters in the core equations, this methodology can be readily adapted to other airports with different ILS configurations.

4 Conclusions

This study addresses the inherent limitations of traditional flight inspection, specifically its intermittency and susceptibility to environmental interference, by establishing a comprehensive simulation

framework that integrates QAR data with high-fidelity navigation modeling. By synthesizing the geometric logic of RNP APCH procedures with the electromagnetic physics of the ILS, this research provides a robust, data-driven methodology for continuous flight quality monitoring.

Three pivotal contributions emerge from the empirical analysis at Linfen Yaodu Airport. First, the development of a site-specific "Digital twin" model effectively bridges the gap between theoretical design and operational reality. Integrating Mercator-projected trajectories with image theory-based signal synthesis enabled the precise reproduction of the complex electromagnetic environment, capturing critical characteristics such as multipath interference and secondary glide slope lobes. Second, a definitive quantitative correlation was established between theoretical signal parameters and pilot instrumentation. Regression analysis revealed a high degree of linearity ($R^2 > 0.98$) between the DDM and the cockpit DOT. This yields a verified calibration equation that translates abstract signal deviations into pilot-centric metrics, significantly enhancing the interpretability of flight data. Third, the framework demonstrated profound utility in forensic investigation. The reconstruction of the June 15, 2023 anomaly successfully traced the causal chain of an unsafe landing, elucidating how a persistent vertical signal deviation propagated through the final approach to cause threshold height exceedance and flare compression.

In summary, this research advances aviation safety by facilitating a transition from periodic, point-based calibration to continuous, trajectory-based analysis. While the current empirical study focuses on a regional airport, the underlying physical and geometric architecture of the framework is inherently scalable. To adapt this "Digital twin" for larger hub airports, future iterations can integrate dynamic multipath models to account for electromagnetic interference caused by complex terminal buildings and denser traffic flows (e.g., taxiing aircraft). Furthermore, by upgrading the image theory module with high-resolution 3D digital elevation models (DEMs), the framework can address a much wider spectrum of topographical multipath challenges. Ultimately, the proposed model offers a scalable solution for verifying route designs, monitoring signal integrity, and preemptively identifying operational risks, thereby providing a scientific foundation for the next generation of flight quality assurance systems.

References

[1] CHEN H, LIU S, XU W Y, et al. Influencing factors of novice pilot SA based on DEMATEL-AISM method: From pilots' view[J]. Heliyon, 2023, 9(2): e13425.

[2] MARK J A, AYAZ H, CALLAN D E. Simultaneous fMRI and tDCS for enhancing training of flight tasks[J]. Brain Sciences, 2023, 13(7): 1024.

[3] FILIP A, RISPOLI F. Continuity of GNSS as a critical attribute for safety applications in land transport[J]. Scientific Reports, 2024, 14(1): 11742.

[4] QIAO Z, YUAN P, HU R, et al. Research on aeromagnetic data error analysis and processing of multi-rotor UAV based on variational mode decomposition algorithm[J]. Heliyon, 2022, 8(11): e11808.

[5] MA Y, ZHU X, LU J, et al. Construction of data-driven performance digital twin for a real-world gas turbine anomaly detection considering uncertainty[J]. Sensors, 2023, 23(15): 6660.

[6] ZHUANG Z, LIN K, ZHANG H, et al. Detection of turbulence anomalies using a symbolic classifier algorithm in airborne quick access record (QAR) data analysis[J]. Advances in Atmospheric Sciences, 2024, 41: 1438-1449.

[7] BASORA L, OLIVE X, DUBOT T. Recent advances in anomaly detection methods applied to aviation[J]. Aerospace, 2019, 6(11): 117.

[8] BRUNTON S L, NATHAN KUTZ J, MANOHAR K, et al. Data-driven aerospace engineering: Reframing the industry with machine learning[J]. AIAA Journal, 2021, 59(8): 2820-2847.

[9] WILLARD J, JIA X, XU S, et al. Integrating scientific knowledge with machine learning for engineering and environmental systems[J]. ACM Computing Surveys, 2022, 55(4): 1-37.

[10] KARNIADAKIS G E, KEVREKIDIS I G, LU L, et al. Physics-informed machine learning[J]. Nature Reviews Physics, 2021, 3(6): 422-440.

[11] BLANCH J, WALTER T, ENGE P, et al. Baseline advanced RAIM user algorithm and possible improvements[J]. IEEE Transactions on Aerospace and Electronic Systems, 2015, 51(1): 713-732.

[12] ZHU L, WANG J, WANG Y, et al. DRL-RNP: Deep reinforcement learning-based optimized RNP flight procedure execution[J]. Sensors, 2022, 22(17): 6475.

[13] KESSLER F C, BATTERSBY S E. Cognition and perception of map projections: A literature review[J]. Cartography and Geographic Information Science, 2024, 51(4): 533-548.

[14] UNKELBACH R M, DAUTERMANN T. Development and evaluation of an RNP AR approach procedure under tight airspace constraints[J]. Aeronautical Journal, 2022, 13(3): 613-625.

[15] PÉREZ S L, MARTÍNEZ GARCÍA-GASCO C, PÉREZ M M, et al. Performance-based navigation approach procedures with barometric vertical guidance: How to select the air temperature for approach procedure design[J]. Aerospace, 2023, 10(4): 337.

[16] KIM T, KAMATH A G, RAHIMI N, et al. Six-degree-of-freedom aircraft landing trajectory planning with runway alignment[J]. Journal of Guidance, Control, and Dynamics, 2025, 48(10): 2225-2242.

[17] PENG Z, LE Y, ZHANG Z H. Design flow and flight safety of RNP-AR flight procedure in civil aviation airport[C]//Proceedings of 2021 IEEE 3rd International Conference on Civil Aviation Safety and Information Technology (ICCASIT). [S.l.]: IEEE, 2021: 1314-1318.

[18] WANG S, MA Y, EASA S M, et al. Sight distance of automated vehicles considering highway vertical alignments and its implications for speed limits[J]. IEEE Intelligent Transportation Systems Magazine, 2023, 16(4): 45-61.

[19] FRITTS Z, BABAEE A, YOUNG S M, et al. Space-time modulation of a multimode electrically small antenna for increased matching and efficiency bandwidths[J]. IEEE Transactions on Antennas and Propagation, 2024, 73(3): 1308-1320.

[20] BO T, KIM H, TAN Z, et al. Optical single-sideband transmitters[J]. Journal of Lightwave Technology, 2022, 41(4): 1163-1174.

[21] ABDULHAMEED A A, KUBÍK Z. Design a compact printed log-periodic biconical dipole array antenna for EMC measurements[J]. Electronics, 2022, 11(18): 2877.

Acknowledgements This work was supported by the National Natural Science Foundations of China (Nos. U2333202,52272351) and the Civil Aviation Capacity Building Fund Project (No. ASSA2024/121).

Authors

The first author Mr. **LIU Jiming** received his B.S. degree and M.S. degree from Nanjing University of Aeronautics and Astronautics (NUAA), Nanjing, China, in 2021 and 2024, respectively. He is currently a research assistant at NUAA. His current research interests are computer vision, machine learning and brain-computer interface (BCI).

The corresponding author Prof. **GAO Zhenxing** received his B.S. degree in vehicle operation engineering from NUAA, Nanjing, China, in 2003, and his Ph.D. degree in civil aircraft operation engineering from NUAA in 2009. From 2009 to 2011, he conducted postdoctoral research in aerospace science and technology at NUAA. He is currently a Professor and Ph.D. supervisor with College of General Aviation and Flight, NUAA. From November 2020 to November 2021, he was a visiting scholar at Imperial College London. His research interests include big data machine learning applications in flight safety, advanced flight control, intelligent flight, mechanism and preventive control of in-flight loss of control, electromechanical control and automation of transportation systems, and complex system dynamics modeling.

Author contributions Mr. **LIU Jiming** and Prof. **GAO Zhenxing** designed the study, complied the models and wrote the manuscript. Mr. **LIU Jiming** and Ms. **LI Yue** conducted the analysis and interpreted the results. Prof. **GAO Zhenxing** provided data and model components for the study, and contributed to the discussion and background of the study. All authors commented on the manuscript draft and approved the submission.

Competing interests The authors declare no competing interests.

(Production Editor: SUN Jing)

高保真进近偏差重构:融合快速存取记录器飞行数据与仪表着陆系统电磁信号物理特性

刘济明[1], 高振兴[2], 李玥[2]

(1.南京航空航天大学民航学院,南京 211106,中国;2. 南京航空航天大学通用航空与飞行学院,南京 211106,中国)

摘要:精准检测进近阶段的飞行轨迹偏差对于识别运行风险和提升航空安全至关重要。但由于缺乏高保真的物理参考模型,现有监测方法在区分环境信号畸变与飞行员操作误差时往往面临巨大挑战。为突破此类局限性,本研究通过将飞行快速存取记录器(Quick access recorder, QAR)数据与严密的导航物理建模相融合,建立了一个涵盖所需导航性能(Required navigation performance, RNP)与仪表着陆系统(Instrument landing system, ILS)进近的综合仿真框架。具体而言,以临汾尧都机场为主要研究对象,构建了一个特定的"数字孪生"模型。首先结合墨卡托投影和气压垂直导航逻辑进行了三维轨迹重建,随后利用天线阵列和镜像理论对ILS信号开展电磁仿真,以准确模拟多径效应。实证检验表明,该模型能够准确复现干涉条纹和次级下滑道波瓣等关键信号特征。在此高保真物理环境的基础上,通过定量回归分析确立了由物理模型推导出的理论调制度差(Difference in depth of modulation, DDM)与飞行员观测到的仪表刻度偏差(Distance off track, DOT)之间存在显著的线性相关性,从而为解释驾驶舱指示数据提供了经过严格验证的校准方程。最终通过对特定垂直偏差异常事件的深度调查,证实了该框架的实用价值:成功追溯了从信号失真到不安全着陆(如高度超限和拉平压缩)之间的因果关系链。本文为持续的飞行品质监控提供了一种稳健的、数据驱动的方法,并为识别导航事故的根本原因提供了科学依据。

关键词:飞行偏差检测;飞行品质监控;RNP进近程序;仪表着陆系统

研究亮点:

1. 建立了一个融合QAR数据与ILS电磁物理特性的综合仿真框架,构建了复杂进近环境的"数字孪生"模型,有效解决了纯数据驱动方法难以区分环境信号畸变与人为操作误差的难题。

2. 深入揭示了理论调制度差与驾驶舱表盘刻度偏差之间的高拟合度线性映射关系,推导并验证了可靠的信号偏差校准方程。

3. 实现了从电磁信号失真到宏观飞行轨迹异常的完整因果链条追溯,为准确识别进近着陆阶段不安全事件的根本原因提供了科学的数据分析支撑。